Over 18% Efficiency from Halogen-Free Solvent-Processed Polymer Solar Cells Enabled by Asymmetric Small Molecule Acceptors with

Downloaded from: https://research.chalmers.se, 2026-11-18 05:49 UTC

Citation for the original published paper (version of record):
Wu, J., Sun, F., Xia, X. et al (2025). Over 18% Efficiency from Halogen-Free Solvent-Processed Polymer Solar Cells Enabled by
Asymmetric Small Molecule Acceptors with Fluoro-Thienyl Extended Terminal. Advanced Functional Materials, 35(24). http://dx.doi.org/10.1002/adfm.202423137

N.B. When citing this work, cite the original published paper.

research.chalmers.se offers the possibility of retrieving research publications produced at Chalmers University of Technology. It covers all kind of research output: articles, dissertations, conference papers, reports etc. since 2004. research.chalmers.se is administrated and maintained by Chalmers Library

(article starts on next page)

Check for updates

ADVANCED FUNCTIONAL MATERIALS
www.afm-journal.de

Over 18% Efficiency from Halogen-Free Solvent-Processed Polymer Solar Cells Enabled by Asymmetric Small Molecule Acceptors with Fluoro-Thienyl Extended Terminal

Jingnan Wu, Fengbo Sun, Xinxin Xia, Leandro R. Franco, Qiaonan Chen, Yúang Fu, Rafael B. Ribeiro, Xinhui Lu, C. Moyses Araujo, Xunchang Wang, Renqiang Yang, Xia Guo, Donghong Yu, Maojie Zhang,* and Ergang Wang**

The potential impact of end-group (EG) in non-fullerene acceptor (NFA) on enabling green solvent-processable polymer solar cells (PSCs) remains underexplored, offering opportunities for advancements in environmentally friendly PSC development. Herein, the EG of 1′,1′-dicyanomethylene-4-fluoro-5-thienyl-3-indanone (IC-FT) is developed by modifying the state-of-the-art of Y6 derivative NFA, BTP-4F, resulting in two novel NFAs, namely BTP-FT and BTP-2FT. Distinctively, this study reveals that it is the noncovalent F···S interaction, other than the commonly believed strong hydrogen bonding of F···H that plays a key role in determining the final molecular conformation, as confirmed by means of 2D NMR study and Gibbs free energy calculations. The asymmetric BTP-FT possesses an upshifted lowest unoccupied molecular orbital level and enhances solubility in toluene. Consequently, it can mitigate phase separation, promote the formation of nanofibrillar morphology, facilitate exciton dissociation, and ultimately enhance the performance of the PSCs, achieving a high open circuit voltage of 0.900 V and a power conversion efficiency (PCE) of 17.56%. Furthermore, the ternary blend PM6:BTP-FT:BTP-4F achieves an enhance PCE of 18.39% in devices processed from toluene. This study offers a novel perspective on NFA design for high-efficiency and eco-friendly processable PSCs by enriching the array of electron-withdrawing EGs on NFA molecules.

1. Introduction

Polymer solar cells (PSCs) represent a promising solar technology for energy conversion due to their flexibility, semi-transparency, and low energy consumption production, making them both cost-effective and environmentally sustainable.[1] In recent decades, substantial advancements in PSCs have achieved remarkable power conversion efficiencies (PCEs) exceeding 19%, largely driven by the development of non-fullerene small molecular acceptors (NF-SMAs).[2] However, most high-efficiency devices currently depend on the use of toxic halogenated solvents (e.g., chloroform/chlorobenzene) during fabrication. This poses significant challenges for the large-scale application of PSCs, as it conflicts with the industry's goal of environmentally friendly and scalable production processes.[3] Therefore, there is an urgent need to develop PSCs that can be fabricated using greener, non-halogenated

J. Wu, L. R. Franco, Q. Chen, E. Wang
Department of Chemistry and Chemical Engineering
Chalmers University of Technology
Göteborg SE-412 96, Sweden
E-mail: ergang@chalmers.se

J. Wu, D. Yu
Department of Chemistry and Bioscience
Aalborg University
Aalborg DK-9220, Denmark
E-mail: yu@bio.aau.dk

The ORCID identification number(s) for the author(s) of this article can be found under https://doi.org/10.1002/adfm.202423137

© 2025 The Author(s). Advanced Functional Materials published by Wiley-VCH GmbH. This is an open access article under the terms of the Creative Commons Attribution-NonCommercial License, which permits use, distribution and reproduction in any medium, provided the original work is properly cited and is not used for commercial purposes.

DOI: 10.1002/adfm.202423137

F. Sun, X. Xia, X. Guo, M. Zhang
National Engineering Research Center for Colloidal Materials
Key Laboratory of Special Functional Aggregated Materials (Shandong University)
Ministry of Education
School of Chemistry & Chemical Engineering
Shandong University
Jinan, Shandong 250100, China
E-mail: mjzhang@sdu.edu.cn

X. Xia, Y. Fu, X. Lu
Department of Physics, Chinese University of Hong Kong
Hong Kong 999077, China

L. R. Franco, C. M. Araujo
Department of Engineering and Physics
Karlstad University
Karlstad 65188, Sweden

solvents. However, non-halogenated solvents often face challenges due to the poor solubility of donor and acceptor molecules, which can result in large-scale phase separation and disordered molecular packing within the active layer. This, in turn, limits the dissociation of excitons and hampers effective charge transport, ultimately reducing device performance.[4]

To address these challenges, researchers have focused on two main strategies: processing techniques and molecular-level modifications. From a processing perspective, methods like high-temperature solution deposition, additives incorporation, and the introduction of a third component have been employed.[5] These approaches promote a nanofibrillar phase-separated morphology and enhance molecular crystallization and orientation within the active layer, thus improving device efficiency. On the molecular level, significant work has been focused on optimizing the solubilizing side chains of NF-SMAs (**Figure** 1a) in their electron-donating cores.[3,4b,6] For example, long, branched 2-decyltetradecyl chains on the dithienothiophen[3,2-b]-pyrrolobenzothiadiazole (TPBT) core achieve improved solubility and suppressed excessive aggregation, leading to optimal phase separation, enhanced hole transport, and reduced non-radiative recombination. These modifications result in higher performance under *o*-xylene processing compared to what Y6 could yield.[6b] However, the role of end-group (EG) modification in PSCs processed with low toxic but satisfied solubility solvents remains underexplored. In chlorinated solvent systems, EG-modifications—such as those on 2-(3-oxo-2,3-dihydroinden-1-ylidene)malononitrile (IC)— are well-known to enhance intermolecular interactions, π-π stacking, and molecular packing, resulting in improved PSC short-circuit current density (J_{sc}) and fill factor (FF).[7] Typical strategies include introducing substituents[7a] (e.g., halogen atom, cyno-, trifluoromethyl-, methoxy-, phenyl-, and halogenated phenyl-group) or fusing aromatic rings[7d–g,8] (e.g., phenyl, thiophene (Th), bicyclic-cyclopentene) onto the benzene ring of IC's (Figure 1a), allowing for fine-tuning optical and electronic properties. Given the versatility of EGs, further investigation into EG modifications compatible with non-halogenated solvents could significantly advance PSC performance and promote eco-friendly processing solutions.

R. B. Ribeiro
Institute of Physics
University of São Paulo
Rua do Matão 1731, São Paulo 05508-090, Brazil
R. B. Ribeiro, C. M. Araujo
Materials Theory Division
Department of Physics and Astronomy
Uppsala University
Uppsala 75120, Sweden
X. Wang, R. Yang
Key Laboratory of Optoelectronic Chemical Materials and Devices (Ministry of Education)
School of Optoelectronic Materials and Technology
Jianghan University
Wuhan 430056, China
D. Yu
Sino-Danish Center for Education and Research
Aarhus DK-8000, Denmark

In this study, we introduced a novel extended EG, designated as 1′,1′-dicyanomethylene-4-fluoro-5-thienyl-3-indanone (IC-FT), by adding one fluorine (F) atom and one Th unit in the commonly used IC EG. Gradual substitution of the IC-2F unit in the reported BTP-4F (or Y6-BO[6a]) with IC-FT yielded two novel NF-SMAs: asymmetric BTP-FT and symmetric BTP-2FT (Figure 1b). Although expanding their molecular sizes typically reduces solubility, the Th moiety, asymmetrically attached to the EG via a C—C bond, effectively alleviates excessive aggregation and the limited crystallinity, significantly enhancing the solubility of BTP-FT nearly threefold in the non-halogenated solvent toluene compared to its original structural analog, BTP-4F. This structural modification significantly mitigates the formation of large phase-separated domains in a fibrous blended film, promoting exciton dissociation, efficient charge transport, and suppressed charge recombination, ultimately enhancing the fill factor (FF) in PM6:BTP-FT-based PSCs. Moreover, devices based on BTP-FT exhibit upshifted lowest unoccupied molecular orbital (LUMO) level, reduced energetic disorder, and improved luminescent efficiency compared to those based on BTP-4F, leading to lower energy loss (E_{loss}) and an ≈11% increase in V_{oc}. Consequently, PM6:BTP-FT-based binary and ternary solar cells achieved notable PCEs of 17.56% and 18.39%, respectively.

Furthermore, density function theory (DFT) calculations revealed accessible noncovalent interactions (NCIs), such as F···H and F···S, between the F atoms on the IC unit and either hydrogen (H) or sulfur (S) atoms in the adjacent Th unit for both SMAs of BTP-FT and BTP-2FT. However, 2D NMR experiments excluded the presence of strong F···H hydrogen bonding but confirmed the sole occurrence of F···S interaction between the IC and Th units. This finding aligns with our reported *O*-conformation of selenophene/Th π-bridge-based dimers, where the S atom on the π-bridge engages in simultaneous interactions with F atoms from neighboring phenyl units, forming F···S interactions on both sites. Such interactions stabilize the conformation of the IC-FT molecule, favoring BTP-FT(b) over BTP-FT(a), as presented in Figure 1c. Notably, we employed a reliable and well-established method for solvation-free energy (ΔG_{solv}) calculations, utilizing molecular dynamics (MD) simulations (details found in Supporting Information), to estimate changes of conformational free energy variances for BTP-xFT molecules in solution (x = 1,2). While traditional implicit solvation methods are widely used, our approach provides better accuracy in capturing the energetic stability of the molecules, which is consistent with our experimental results.

2. Results and Discussion

The synthetic pathways of the precursors and the final target compounds are outlined in Scheme S1 (Supporting Information). The precursors, BTP-3FBr and BTP-2F2Br, were synthesized via one-pot Knoevenagel reactions between the core unit BTPBO-CHO and two different EGs (IC-2F and IC-FBr (1:1 for BTP-FBr) or the latter solely for BTP-2F2Br, respectively. These were then separated by means of column chromatography. Subsequently, BTP-FT and BTP-2FT were obtained via Pd-catalyzed Stille coupling reactions between asymmetric monobrominated BTP-3FBr or symmetric brominated BTP-2F2Br, and mono-stannylated thiophene, respectively. Detailed procedures

© 2025 The Author(s). Advanced Functional Materials published by Wiley-VCH GmbH

16163028, 2025, 24, Downloaded from https://advanced.onlinelibrary.wiley.com/doi/10.1002/adfm.202423137 by Statens Beredning, Wiley Online Library on [13/08/2025]. See the Terms and Conditions (https://onlinelibrary.wiley.com/terms-and-conditions) on Wiley Online Library for rules of use; OA articles are governed by the applicable Creative Commons License

and analytical results are described in the experimental section in Supporting Information. Both the intermediate and the final target molecules were characterized using ^{1}H NMR, ^{13}C NMR, and Matrix-Assisted Laser Desorption/Ionization Time of Flight Mass Spectrometry (MALDI-TOF MS). Additionally, thermogravimetric analysis (TGA) was conducted under a nitrogen atmosphere to assess the thermal stability of the compounds, revealing high onset decomposition temperatures exceeding 320 °C at a weight loss of 5% (Figure S1, Supporting Information). To further understand the electronic structure of the new NFAs, we performed DFT calculations using the B3LYP exchange-correlation functional and the long-range corrected OT-LCωHPBE functional. The latter was optimally tuned to describe the electronic properties of these molecules in their specific organic semiconductor environments.[9] Methodological details are available in Supporting Information.

The Th ring and the IC unit in BTP-FT and BTP-2FT may undergo rotation along the single C—C bond between the two bridging C atoms, resulting in potentially different conformations.[10] To explore this, a relaxed potential electronic energy scan was conducted for the rotation of the terminal Th ring in BTP-FT (Figure 1c). Two distinct minima with an energy difference of 0.13 kcal mol^{-1} were identified, separated by an energetic barrier of 3.3 kcal mol^{-1}. These results were obtained using the B3LYP-GD3BJ/6-311G(d,p) theoretical level, incorporating implicit solvent effects via the polarizable continuum model (PCM) model. At this theory level, the conformation with the S atom oriented toward F (S···F) is slightly more stable than the conformation with the H oriented toward the F (H···F). Table S1 (Supporting Information) presents a detailed analysis of conformational stability, incorporating thermal corrections to Gibbs-free energy and ΔG_{solv} derived from MD simulations using the Bennet acceptance ratio (BAR)-MD method. The results show that, when explicit solvent effects are included through MD simulations, the stability difference between conformations becomes more pronounced. Specifically, the BAR-MD method revealed an energy increase ($G_{SOL(a)} - G_{SOL(b)}$, from the S···F conformation to the H···F conformation) of 0.60 kcal mol^{-1} for BTP-FT and 0.74 kcal mol^{-1} for BTP-2FT, respectively. The fractional population distribution of the two conformers follows the Boltzmann distribution, expressed as $(1+exp(-\Delta G/K_B T))^{-1}$, where ΔG is the free energy difference between the two conformations in solution, K_B is the Boltzmann constant, and T is the temperature (298.15 K). Thus, considering the energetic balance between H···F and S···F conformers, our calculations present a fraction population of 73% and 78% of S···F conformation for BTP-FT and BTP-2FT molecules in chloroform solution, respectively. Interestingly, the asymmetric conformation in the case of BTP-2FT is the least stable one and would rarely be accessible, as seen in Table S1 and Figure S2 (Supporting Information) for more details.

To confirm the intrinsic intramolecular NCIs and resulting conformations, we conducted a detailed analysis of 2D NMR (^{1}H-^{1}H Nuclear Overhauser Effect Spectroscopy (NOESY)) spectra. All aromatic protons of the two SMAs were labeled from H_a to H_i for BTP-FT, and from H_a to H_f for BTP-2FT, as shown in Figure S3 (Supporting Information). Estimated inter-proton distances between adjacent ones from H_a to H_e in the two different conformations are summarized in Table S2 (Supporting Information). As illustrated in Figures 1d and S4 (Supporting Information), notable NOE correlations such as H_a-H_b, H_b-H_c, H_c-H_d, and H_d-H_e were observed in both BTP-FT and BTP-2FT when the protons were within a distance of 5 Å.[11] This suggests exchange cross-peaks between the protons of Th (H_b and H_c) and adjacent phenyl protons (H_d and H_e) in the two acceptors, indicating the presence of the conformation of BTP-FT(b). Analyzing the interatomic distances of F···H and F···S in both SMAs revealed values of 2.32 and 2.76 Å, respectively (Table S3, Supporting Information). These distances are shorter than the sum of their van der Waals radii of F-H (2.53 Å) and F-S (3.10 Å), confirming the existence of non-covalent F···H and F···S intramolecular interactions in BTP-xFT(a) and BTP-xFT(b)-based isomers (x = 1 or 2), respectively. Additionally, the lower-energy isomer based on the latter displays a smaller average dihedral angle of 5.5° compared to that of 21.0° for the former, which promotes more favorable intermolecular stacking. While both conformations (H···F and S···F) are theoretically accessible, our experimental highlights the significant role of the noncovalent F···S interaction between the F atom in the IC unit and the S atom in the adjacent Th unit, which is essential in determining the conformation of the EG IC-FT unit. This finding aligns with our previously reported distinctive *O*-shape molecular conformations of dimeric acceptors, which were experimentally determined by 2D NMR for the first time.[10a] These conformations are characterized by F···S/Se interactions, rather than strong hydrogen bonding F···H forces.

When running theoretical calculations, it is crucial to understand that the energetic stability of the H···F and S···F conformations is highly dependent on chemical-/physical-environmental effects. In the gas phase, the calculated Gibbs free energy difference between these conformers varies by less than 0.08 kcal mol^{-1}, indicating the coexistence of both conformations in a thermodynamic equilibrium of ≈50%/50%. This equilibrium is altered by the presence of the solvent, which preferentially stabilizes the S···F conformation. The S···F conformation has a slightly higher dipole moment than the H···F conformation for both BTP-FT (μ_{HF} = 5.6 D, μ_{SF} = 6.7 D) and BTP-2FT (μ_{HF} = 9.6 D, μ_{SF} = 10.4 D), as calculated using B3LYP-GD3BJ/6-311G(d,p) in gas phase (Figure S5, Supporting Information). The increased dipole moment enhances its stability in chloroform solution, a polar solvent where electrostatic interactions play a significant role. Preferential stabilization of the S···F conformation is observed even when treating the solvent implicitly using a dielectric-based approach, such as the PCM. However, the BAR-MD method (see Supporting Information) provides a discrete and more detailed description of solvation, capturing specific solute-solvent interactions, entropy changes, and other dynamic and statistical aspects of solvation. This method corroborates our experimental findings that the S···F conformation is indeed the most stable and prevalent one adopted by BTP-xFT molecules in chloroform solution.

Based on the determined F···S NCI within SMAs, we calculated the electrostatic surface potential (ESP) distribution of IC-FT and compared it with that of IC-2F. As illustrated in Figure 1e, the introduction of the Th unit leads to a decrease in ESP values across the surface of IC-FT, making it less positive. This decline is observed for all carbon, hydrogen, oxygen, and nitrogen atoms within the IC, arising from the electron-donating properties of the Th unit, which effectively raises the molecular energy levels

© 2025 The Author(s). Advanced Functional Materials published by Wiley-VCH GmbH

16163028, 2025, 24, Downloaded from https://advanced.onlinelibrary.wiley.com/doi/10.1002/adfm.202423137 by Statens Beredning, Wiley Online Library on [13/08/2025]. See the Terms and Conditions (https://onlinelibrary.wiley.com/terms-and-conditions) on Wiley Online Library for rules of use; OA articles are governed by the applicable Creative Commons License

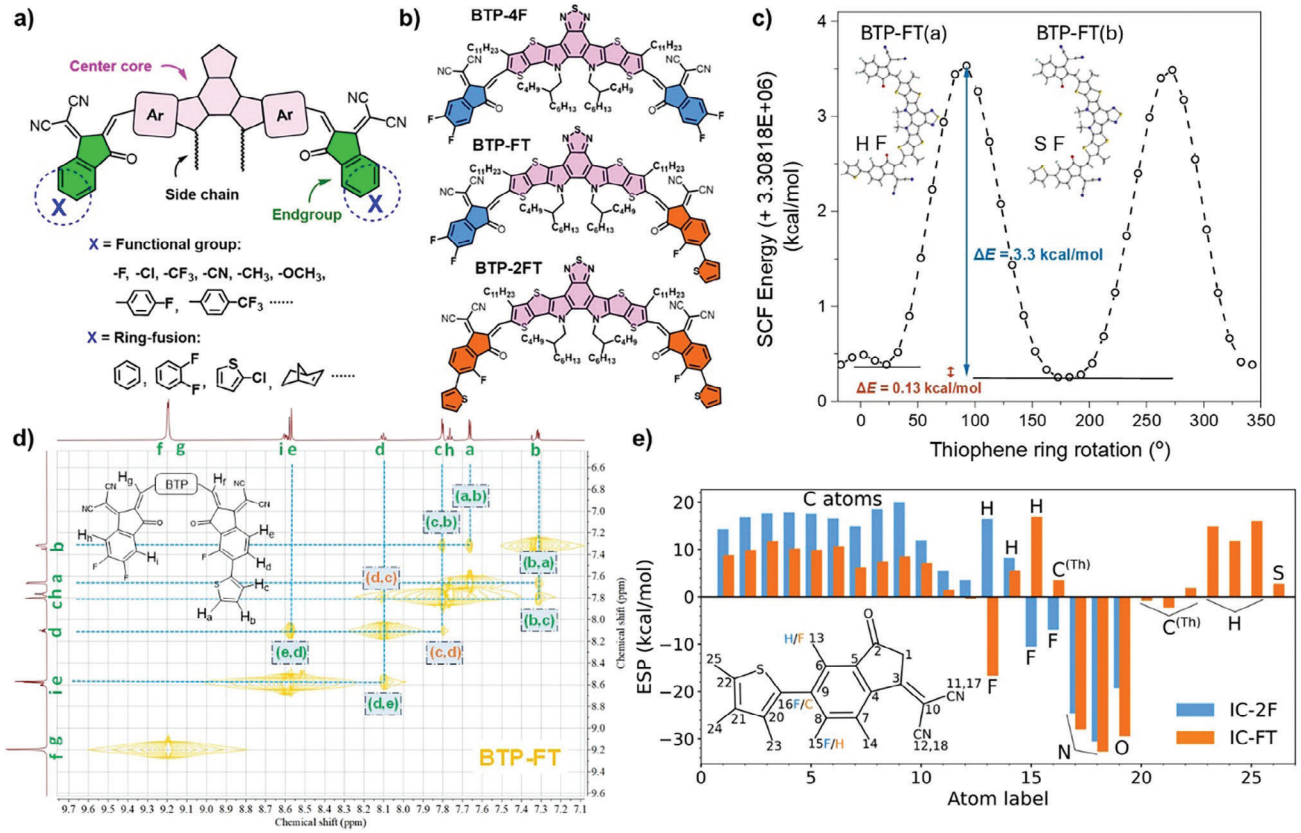

Figure 1. a) Schematic structures of EG-engineered NF-SMAs. b) Chemical structures of BTP-4F, BTP-FT, and BTP-2FT. c) B3LYP-GD3BJ/6-311G(d,p) potential energy scans, resulting from the rotation of the ending thiophene ring of BTP-FT in chloroform solution via PCM model. d) ^{1}H-^{1}H 2D NMR spectrum (700 MHz) of BTP-FT in $C_2Cl_4D_2$ solution at 313 K. e) Average atomic electrostatic surface potential (ESP) of IC-FT and IC-2F calculated at OT-LCωHPBE/6-311+G(d,p) theory level.

(Figure S6 and Table S4, Supporting Information). In the cyclic voltammetry (CV) measurements (Figure S7, Supporting Information; Figure 2b), it is apparent that the HOMO energy level remains relatively stable, fluctuating slightly within the range of ≈5.95–6.04 eV. Conversely, the LUMO energy levels exhibit a notable upward shift from BTP-4F to BTP-2FT, with calculated values of ≈−4.23, −4.17, and −4.15 eV, respectively. These upshifts in the LUMO levels suggest that higher V_{oc} can be obtained from their respective devices.

We further analyzed the solubility properties of SMAs in toluene to facilitate device processing in a non-halogenated solvent. Solubility was assessed by measuring the saturated solubility (S_{45}) in toluene at 45°C.[4a] Absorption spectra of the dilute toluene solutions at known concentrations are presented in **Figures** 2e and S8 (Supporting Information). Generally, larger conjugated molecules exhibit lower solubility than their parental small molecules when the length of the bulk alkyl chains remains constant. However, upon incorporating Th into one of two terminals, the solubility of the resulting SMA BTP-FT increased nearly threefold, from 29.8 (for BTP-4F) to 81.7 mg mL^{-1} (for BTP-FT). By contrast, the introduction of Th on both terminals significantly decreased the solubility to 8.5 mg mL^{-1} (for BTP-2FT). This finding highlights the role of asymmetry-controlled A-D-A or A-D-A′-D-A configurations with non-fused Th in enhancing their solubilities.

To investigate the impact of non-fused Th incorporation on molecular crystallinity, and thus solubility, we conducted grazing incidence wide-angle X-ray scattering (GIWAXS) measurements[12] (Figure 2d; Figure S9, Supporting Information). The crystal coherence length (CCL^{oop}) of 1.84 nm for BTP-FT in its out-of-plane (OOP) direction was determined, as being shorter than that of 2.28 nm for BTP-4F (Figure 2e). Furthermore, BTP-FT showed relatively subtle and broad full width at half maximums (FWHMs) for both lamellar stacking and EG π–π staking peaks at ≈0.29 and ≈0.33 Å, respectively, in the in-plane (IP) direction. These both suggest that the effective breaks of the backbone by unfused Th and molecular symmetry mitigate over-aggregation and crystallinity in BTP-FT, consequently enhancing its solubility. However, for BTP-2FT, the symmetric Th-incorporation enhanced its crystallinity (CCL^{oop} = 2.78 nm), with a sharper lamellar stacking peak, resulting in larger crystal sizes and therefore decreased solubility.

Additionally, we also carried out theoretical calculations on the solvation effects of three NFAs in toluene to evaluate the solubility of BTP-4F, BTP-FT, and BTP-2FT using two key parameters: formation energy (FE) and soΔG_{solv}. These calculations were performed at the B3LYP/6-311G(d,p) level with GD3BJ empirical dispersion correction and the SMD model to account for toluene solvent effects. The results are presented in Table S6 and

© 2025 The Author(s). Advanced Functional Materials published by Wiley-VCH GmbH

16163028, 2025, 24, Downloaded from https://advanced.onlinelibrary.wiley.com/doi/10.1002/adfm.202423137 by Statens Beredning, Wiley Online Library on [13/08/2025]. See the Terms and Conditions (https://onlinelibrary.wiley.com/terms-and-conditions) on Wiley Online Library for rules of use; OA articles are governed by the applicable Creative Commons License

16163028, 2025, 24, Downloaded from https://advanced.onlinelibrary.wiley.com/doi/10.1002/adfm.202423137 by Statens Beredning, Wiley Online Library on [13/08/2025]. See the Terms and Conditions (https://onlinelibrary.wiley.com/terms-and-conditions) on Wiley Online Library for rules of use; OA articles are governed by the applicable Creative Commons License

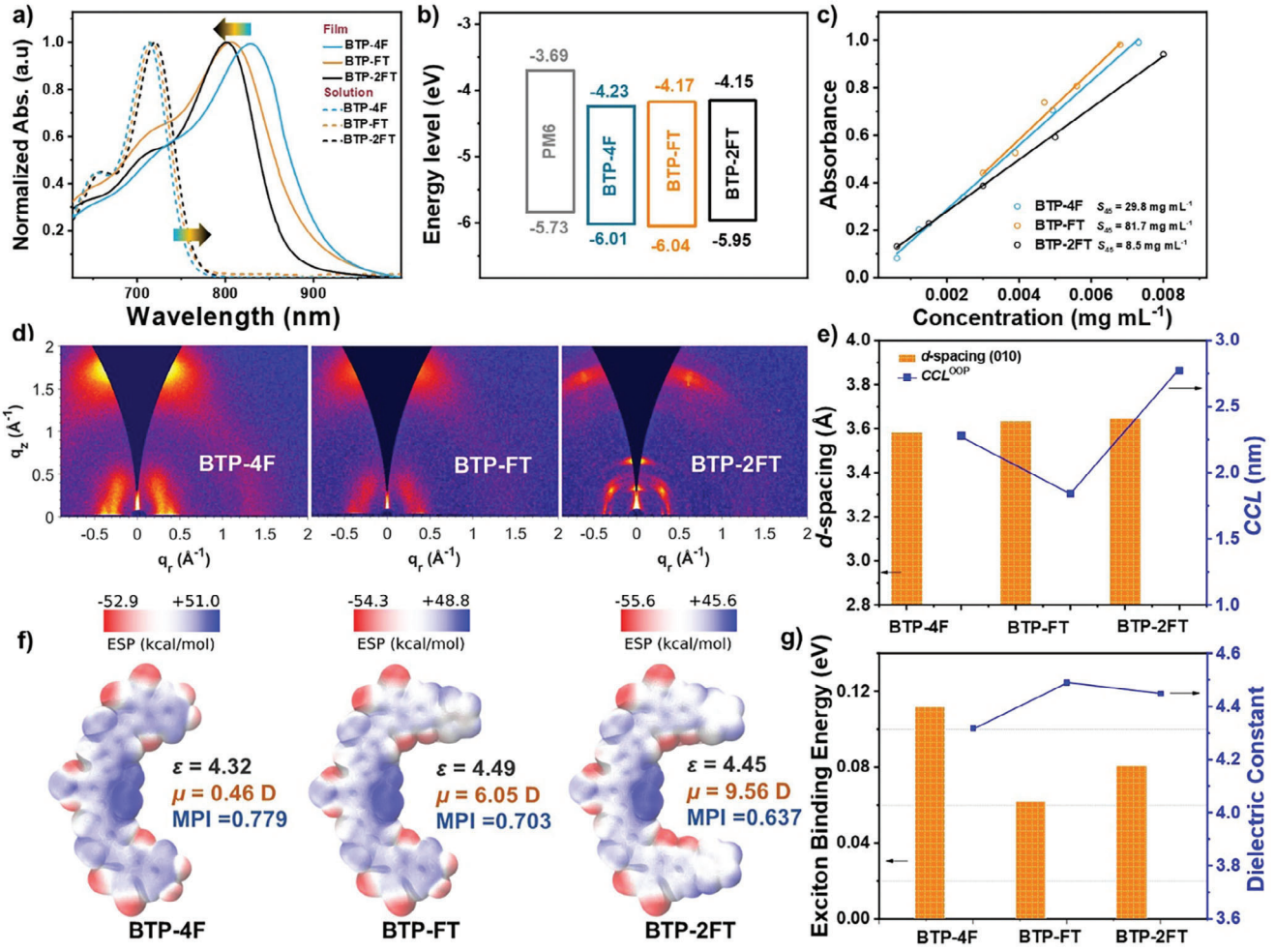

Figure 2. a) Normalized UV–vis absorption spectra of three SMAs in both chloroform solution and pristine films. b) Energy level alignment of PM6, BTP-4F, BTP-FT, and BTP-2FT, respectively. c) Concentration dependency on molecular absorbance of diluted toluene solutions of BTP-4F, BTP-FT, and BTP-2FT and obtained S_{45} values of theirs. 2D GIWAXS patterns and corresponding e) CCL^{OOP}, and *d*-spacing (010) values of the pristine acceptor films. f) ESP distribution, g) exciton binding energy at the OT-LCwHPBE/6-311+G(d,p) level of theory and dielectric constants determined via Clausius–Mossoti equation of BTP-4F, BTP-FT and BTP-2FT molecules.

Figure S10 (Supporting Information). FE corresponds to the difference in energy between the dimer interface and two times the single molecule, while the ΔG_{solv} is the difference between the system in vacuum and solvated in toluene. In practice, the former reflects the tendency of molecules to aggregate into dimers or larger structures, whereas the latter indicates the stability of molecules or aggregates in solution. The detail of reliable interface models is shown in Supporting Information. The negative FE/N values (normalized by the number of atoms) for all three systems indicate a tendency to form dimers or larger aggregates in solution. The similarity in FE/N values among BTP-4F, BTP-FT, and BTP-2FT suggests comparable aggregation tendencies across these molecules. For the most stable dimers, the ΔG_{solv}/N values are the following: −0.333 kcal mol^{-1} atom^{-1} for dimer 2 (BTP-FT), −0.344 kcal mol^{-1} atom^{-1} for dimer 7 (BTP-2FT), and −0.334 kcal mol^{-1} atom^{-1} for dimer 9 (BTP-4F). Based on these normalized values, the theoretical solubility trend aligns more closely with experimental observations: BTP-FT > BTP-4F > BTP-2FT, with BTP-2FT being the least soluble.

Furthermore, it was observed that the introduction of Th leads to a slightly increased π–π stacking distances (*d*-spacing (010)) from 3.59 Å for BTP-4F to 3.64 Å for BTP-FT and 3.65 Å for BTP-2FT. This disruption of interchain interactions could be attributed to not only the twisted Th but also potentially their intrinsic electrostatic interactions. As shown in Figure 2f, the introduction of Th leads to an overall increase in the negativity of the ESPs. The extremely positive and negative ESP values change from −52.9/51.0 kcal mol^{-1} in BTP-4F to −54.3/48.8 kcal mol^{-1} in BTP-FT and −55.6/45.6 kcal mol^{-1} in BTP-2FT. Regarding electrostatic interactions, the intermolecular interaction among BTP-4F molecules is larger compared to those among the others. Therefore, the decrease of these interactions may be contributed to the slightly increased π–π stacking distances upon Th substitution, which is indicated by their declined ESP extremes (2704.1, 2649.9, and 2537.5 kcal mol^{-1}) or their surface molecular polarity index (MPI) indexes (0.779, 0.703, and 0.637 eV) for BTP-4F, BTP-FT, and BTP-2FT, respectively. Interestingly, among the acceptors, BTP-FT presents the smallest exciton binding energy

 © 2025 The Author(s). Advanced Functional Materials published by Wiley-VCH GmbH

16163028, 2025, 24, Downloaded from https://advanced.onlinelibrary.wiley.com/doi/10.1002/adfm.202423137 by Statens Beredning, Wiley Online Library on [13/08/2025]. See the Terms and Conditions (https://onlinelibrary.wiley.com/terms-and-conditions) on Wiley Online Library for rules of use; OA articles are governed by the applicable Creative Commons License

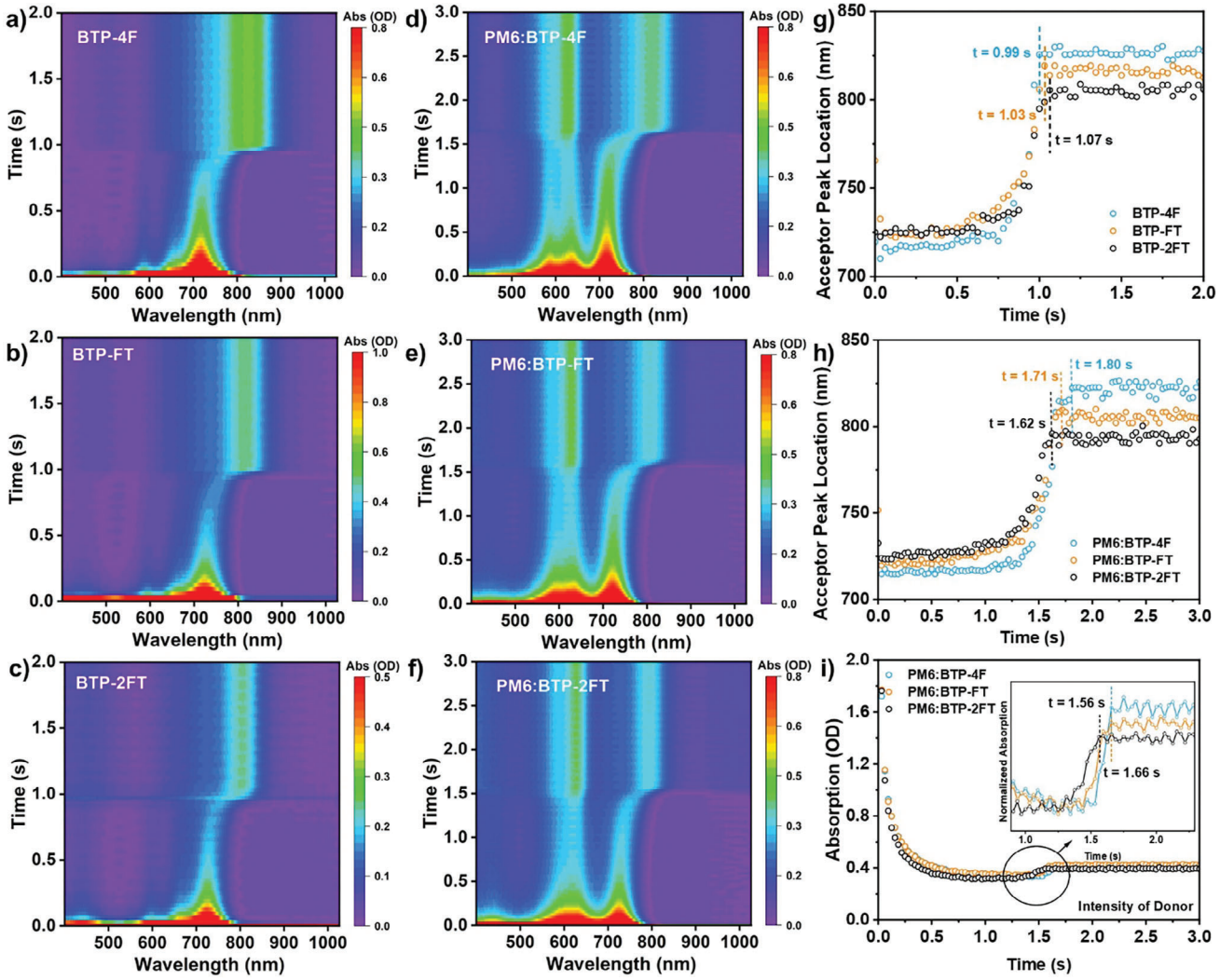

Figure 3. a–c) Time-dependent contour maps of the in situ UV–vis absorption spectra of BTP-4F, BTP-FT, and BTP-2FT, respectively, and d–f) corresponding to their PM6-based blend films. g–i) Time evolution of the absorption of the three acceptors and their blend system with PM6.

(E_{BE}) of 0.062 eV, as obtained with the OT-LCωHPBE method. This is compatible with the highest dielectric constant ($\epsilon = 4.49$) of the material predicted by the Clausius–Mossotti equation (see Table S4, Supporting Information). Within a simplified model of electron-hole Coulomb interaction, binding energies decrease as ε increases, facilitating exciton dissociation at lower E_{BE} values.

In situ UV–vis measurements provided insights into the kinetic differences in the film formation for both the acceptors and their blend systems.[13] As shown in **Figure 3**a–f, during the initial solvent evaporation stage (<0.5 s), we observed a redshift in the absorption peaks from BTP-4F to BTP-2FT for both the neat and blend films, aligning with their spectra recorded in solutions (Figure 2a; Table S5, Supporting Information). This redshift has been primarily resulted from extended conjugation due to the introduction of Th. Despite similar overall film formation time among the three acceptors, Th-based SMAs show smaller redshifts compared to BTP-4F after solvent evaporation (>1.1 s). This difference in redshift suggests reduced intermolecular π–π stacking in the Th-containing acceptors, as evidenced by the offset of the acceptors (Figure 3g,h) and the changes in peak/onset wavelengths (Figure 2a). These observations align with our previous findings on solubility and aggregation behavior, highlighting that the introduction of Th effectively reduces over-aggregation and crystallinity, leading to distinct molecular packing characteristics and weaker π–π stacking in BTP-FT film relative to BTP-4F.

Moreover, we found that, when blended with the donor polymer PM6, the film drying times of the acceptor materials shifted from those observed in the neat films. Notably, BTP-2FT, which initially demonstrated the longest drying time among three neat films (Figure 3g), exhibited the shortest time in its blend film (Figure 3h), while BTP-4F in the PM6-based blend had the longest drying time (Figure 3h). This suggests an influence of donor–acceptor compatibility on the film drying process. To investigate this, we performed contact angle measurements (Figure S11, Supporting Information) to estimate the surface energies (γ) (Table S7, Supporting Information) of PM6 and the three

 © 2025 The Author(s). Advanced Functional Materials published by Wiley-VCH GmbH

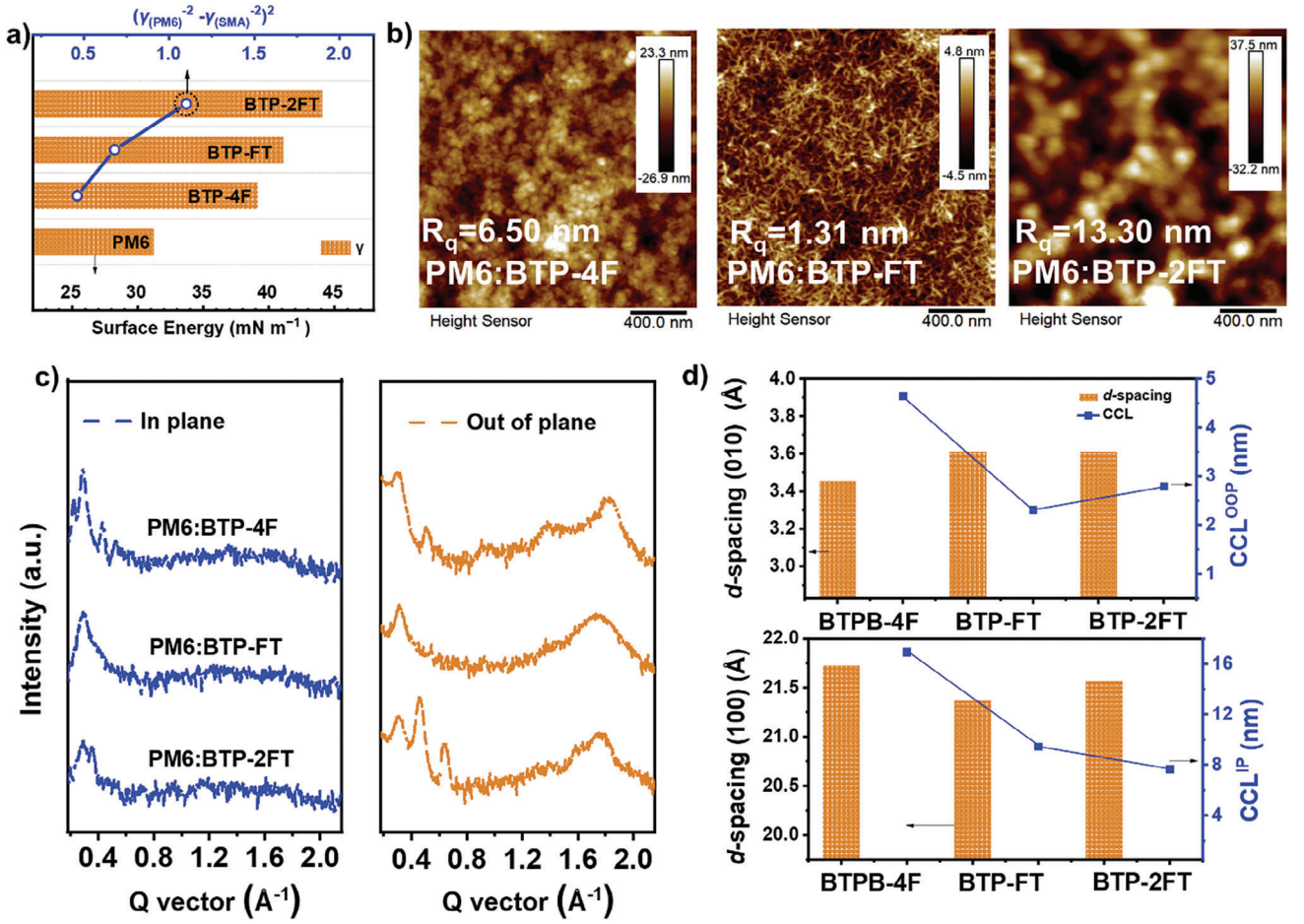

Figure 4. a) Surface tension of PM6, BTP-4F, BTP-FT, and BTP-2FT neat films. b) Tapping mode AFM topography height-image of PM6:BTP-4F, PM6:BTP-FT, and PM6:BTP-2FT blend films. c) 1D line cuts of PM6:BTP-BO-4F, PM6:BTP-FT, and PM6:BTP-2FT blend films. d) The CCL^{OOP}, *d*-spacing (010) CCL^{IP}, and *d*-spacing (100) values of three blend films from 2D GIWAXS. e) Schematic presentation of the morphology for the PM6-based blend films.

acceptors, quantifying the compatibility between two materials (i and j) with the equation $(\sqrt{\gamma_i}\text{-}\sqrt{\gamma_j})^2$.[14] The values obtained were 0.46, 0.68, and 1.10 for PM6:BTP-4F, PM6:BTP-FT, and PM6:BTP-2FT, respectively (**Figure** 4a), indicating decreased miscibility in such an order. The low solubility and reduced compatibility of BTP-2FT with PM6 result in an early phase separation of the donor (shortest film forming time in Figure 3i) and acceptor during film formation. Thus, an uneven morphology with relatively large phase separation occurred, as proven by atomic force microscopy (AFM) images in Figure 4b and the transmission electron microscopy (TEM) image in Figure S12 (Supporting Information). Unlike the single non-fused Th-based acceptor BTP-FT, which formed fibrillar domains, the highest miscibility observed between the PM6:BTP-4F mixture presented a rougher surface due to its inherently stronger crystallinity (discussed further in the GIWAXS results, Figure 4c,d) and longer crystal growth time (Figure 3h), potentially suppressing exciton dissociation and partly hindering their enhancement of FF and J_{sc} in the resulting devices.

GIWAXS measurements were conducted to gain deeper insights into the influence of Th substitution on molecular ordering, crystallinity, and molecular texture characteristics of the blends at the nanometer scale (Figure S12, Supporting Information). All three blend films exhibited a clearly pronounced face-on orientation with π–π diffraction peaks (010) ranging from 1.73 to 1.81 Å in the OOP direction and a lamellar peak (100) at ≈0.29 Å in the IP direction. As illustrated in Figure 4d, the solubility of the materials also influenced the crystal features in the three blends, consistent with observations in their neat films. Specifically, the PM6:BTP-FT blend demonstrated the lowest CCL^{oop} value and a moderate *d*-spacing (010). Notably, the highly miscible BTP-4F-based mixture, processed in toluene, displayed robust crystallinity in both IP and OOP directions. With its longer film formation time, BTP-4F resulted in larger crystallized regions, causing excessive phase separation from the donor (Figure S13, Supporting Information). In contrast, the PM6 in BTP-FT-based blend retained relatively high crystallinity, similar to BTP-4F system, in the IP direction with tight lamellar stacking, which likely contributed to enhanced charge transport properties in the blended films. These findings unequivocally underscore that the introduction of the Th substituent significantly alters the molecular stacking properties of the SMAs.

© 2025 The Author(s). Advanced Functional Materials published by Wiley-VCH GmbH

16163028, 2025, 24, Downloaded from https://advanced.onlinelibrary.wiley.com/doi/10.1002/adfm.202423137 by Statens Beredning, Wiley Online Library on [13/08/2025]. See the Terms and Conditions (https://onlinelibrary.wiley.com/terms-and-conditions) on Wiley Online Library for rules of use; OA articles are governed by the applicable Creative Commons License

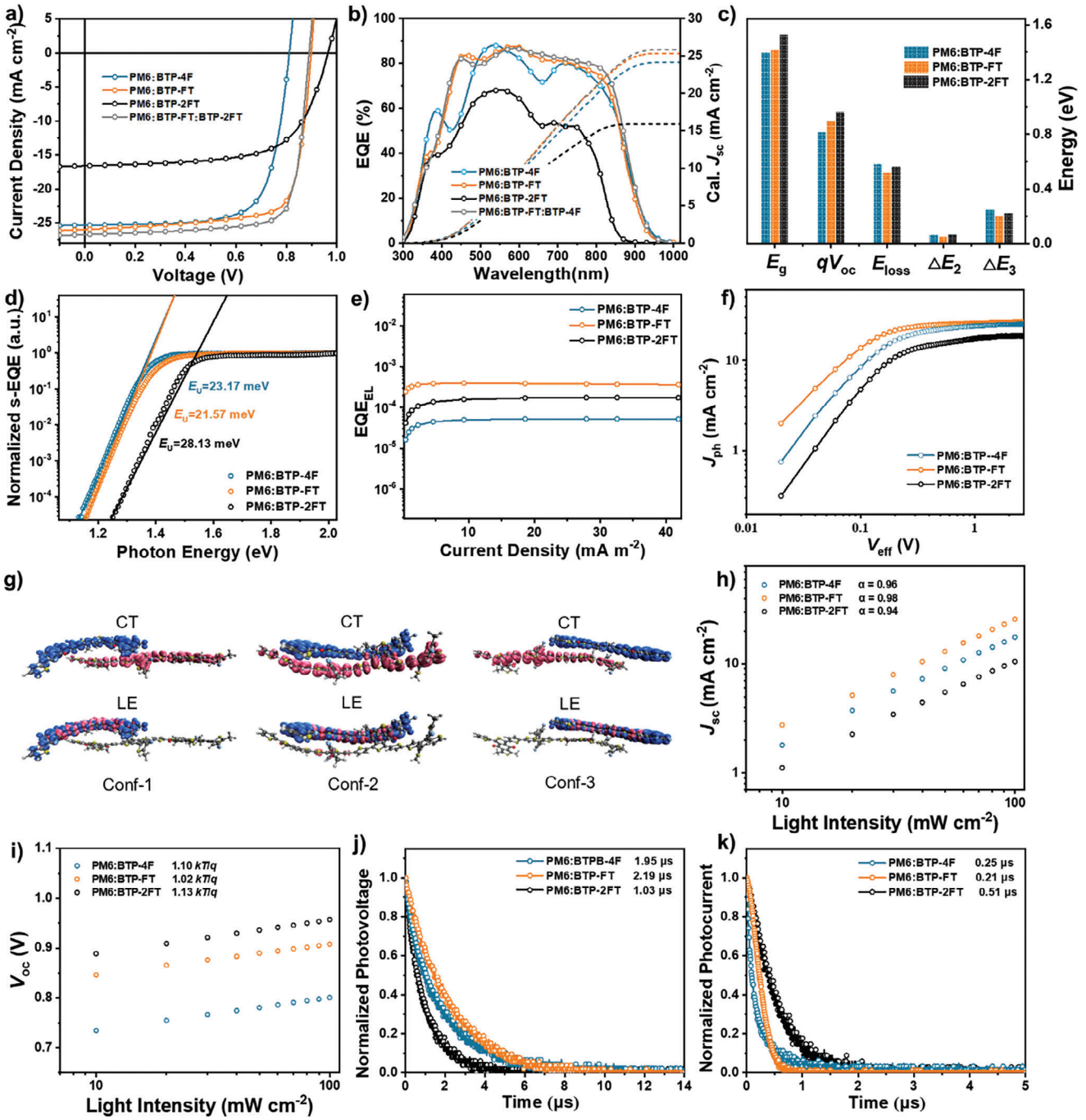

Figure 5. a) *J*–*V* characteristics and b) EQE curves and integrated J_{sc} values for optimized devices based on binary PM6:SMAs and ternary PM6:BTP-FT:BTP-4F (1:1:0.3, weight ratio), respectively. c) Energy loss analysis diagram, d) normalized s-EQE, e) luminescence efficiency EQE_{EL} data for the optimized PM6-based devices. f) Characteristics of J_{ph} versus V_{eff} for the optimized PM6-based devices. g) Electron (blue color) and hole (pink color) isosurfaces of the local exited (LE) state and charge transfer (CT) state for three conformations of the interface BTP-FT/PM6. The dependence of h) J_{sc} and i) V_{oc} on light intensity. j) normalized transient photovoltage (TPV), and k) transient photocurrent (TPC) data for the optimized PM6-based devices.

PSCs were fabricated using a conventional device structure: ITO/poly(3,4-ethylenedioxythiophene):poly(styrene sulfonate) (PEDOT:PSS)/active layer/poly[(9,9-bis(3′-((N,N-dimethyl)-N-ethylammonium)-propyl)-2,7-fluorene)-2,7-fluorene)-alt-2,7-(9,9-dioctylfluorene)]dibromide (PFN-Br)/Ag with toluene as a halogen-free solvent. The state-of-the-art donor polymer PM6 was chosen as the electron donor based on its well-matched energy levels with these acceptors. **Figure** 5a presents the current density–voltage (*J*–*V*) characteristics of the champion PSCs, which were finely turned by varying the amounts of additives, thermal annealing-temperature, and -time (Figure S14 and Tables S8–S10, Supporting Information). As shown

© 2025 The Author(s). Advanced Functional Materials published by Wiley-VCH GmbH

16163028, 2025, 24, Downloaded from https://advanced.onlinelibrary.wiley.com/doi/10.1002/adfm.202423137 by Statens Beredning, Wiley Online Library on [13/08/2025]. See the Terms and Conditions (https://onlinelibrary.wiley.com/terms-and-conditions) on Wiley Online Library for rules of use; OA articles are governed by the applicable Creative Commons License

Table 1. Photovoltaic performance of the PSCs based on PM6: acceptor (1:1.2, w/w) under the illumination of AM 1.5 G, 100 mW cm^{-2}.

D:A	V_{oc} [V]	J_{sc} [mA cm^{-2}]	Cal. J_{sc}[a)] [mA cm^{-2}]	FF [%]	PCE$_{max}$[b)] [%]
PM6:BTP-4F	0.812	25.31	24.19	72.5	14.90 (14.75 ± 0.19)
PM6:BTP-FT	0.900	25.95	25.32	75.2	17.56 (17.41 ± 0.12)
PM6:BTP-2FT	0.966	16.49	15.91	65.0	10.35 (10.26 ± 0.10)
PM6:BTP-FT:BTP-4F[c)]	0.890	26.70	25.86	77.4	18.39 (18.17 ± 0.17)

[a)] Integral J_{sc} calculated from the EQE curves; [b)] The average PCE values in brackets were obtained from 15 devices; [c)] PM6:BTP-FT:BTP-4F (1:1:0.3, weight ratio).

in **Table 1**, the optimal device utilizing BTP-FT demonstrated an outstanding PCE of 17.56%, characterized by a high V_{oc} of 0.900 V, a J_{sc} of 25.95 mA·cm^{-2}, and an FF of 75.2%. This performance surpassed that of the device utilizing BTP-4F (PCE: 14.90%, V_{oc}: 0.812 V, J_{sc}: 25.31 mA·cm^{-2}, FF: 72.5%). Although the BTP-FT device exhibited a blueshifted absorption compared to the BTP-4F neat (Figure 2a) and corresponding blend films (Figure S15, Supporting Information), it did not compromise the J_{sc}. Conversely, the BTP-2FT-based device exhibited a reduced PCE of 10.26% (V_{oc}: 0.966 V, J_{sc}: 16.49 mA·cm^{-2}, FF: 65.0%). To further improve the J_{sc}, BTP-4F (as 30 wt.%, refer to another acceptor as 100 wt.%) was added to the blend of PM6:BTP-FT to construct a ternary device for enhancing the optical absorption of the active layer, which delivered an improved PCE of 18.39% with simultaneous increases in J_{sc} (26.70 mA cm^{-2}) and FF (77.4%), representing one of the highest PCEs for toluene-processing PSCs (Table S11, Supporting Information). Figure 5b illustrates the external quantum efficiency (EQE) spectra of these devices, which revealed strong photon responses in the optical region from 400 to 900 nm for all four devices. The devices based on PM6:BTP-4F and PM6:BTP-FT showed a notably higher light response, with maximum EQEs exceeding 80%, compared to those based on BTP-2FT. This difference was a contributing factor to the higher J_{sc} observed in the former devices. In addition, incorporating BTP-4F to PM6:BTP-FT is beneficial for extending the EQE response. The integrated J_{sc} from the EQE curves are 24.19, 24.81, 15.91, and 25.46 mA cm^{-2} for the PSCs based on binary BTP-4F, BTP-FT, and BTP-2FT, and ternary PM6:BTP-FT:BTP-4F blends, respectively, which is consistent with the J_{sc} values from the J–V curves within 4% deviation, affirming the accuracy of the J–V measurements.

Achieving a high V_{oc} (see Figure S16, Supporting Information) with low voltage loss is highly desirable for PSCs. Thus the significant improvement in V_{oc} for devices based on acceptors adopting Th is noteworthy and requires further investigation. Primarily, this improvement arises from the increased LUMO energy level of these acceptors (Figure 2b). Furthermore, it is closely related to voltage loss (i.e., E_{loss}) within the devices, which can be quantified by using the following formula:[15] $E_{loss} = (E_g - qV_{oc}) = (E_g - qV_{oc}^{SQ}) + (qV_{oc}^{SQ} - qV_{oc}^{rad}) + (qV_{oc}^{SQ} - qV_{oc}) = (E_g - qV_{oc}^{SQ}) + q\triangle V_{oc}^{rad,\ below\ gap} + q\triangle V_{oc}^{non\text{-}rad} = \triangle E_1 + \triangle E_2 + \triangle E_3$, whereas E_g is the bandgap, q is the elementary charge, V_{oc}^{SQ} is the maximum voltage under the Shockley–Queisser (SQ) limit, and V_{oc}^{rad} is the V_{oc} when only radiative recombination is taken into consideration. $\triangle V_{oc}^{rad,\ below\ gap}$, is the voltage loss of radiative recombination from the absorption below the bandgap and $\triangle V_{oc}^{non\text{-}rad}$ is the voltage loss of non-radiative recombination. $\triangle E_1$ represents an unavoidable component, due to radiative recombination from absorption above the bandgap. $\triangle E_2$ is influenced by the reorganization energy and energy disorder degree of the blends, due to radiative recombination from absorption below the bandgap. $\triangle E_3$ is quantitatively related to the luminescence efficiency of photovoltaic materials, due to non-radiative recombination, and can be obtained by using the formula: $\triangle E_3 = q\triangle V_{oc}^{non\text{-}rad} = -kT\ln(EQE_{EL})$, where k is the Boltzmann constant, T is the Kelvin temperature, and EQE_{EL} is the electroluminescence (EL) quantum efficiency of the device when charge carriers are injected into the device in the darkness. The detailed E_{loss} values are presented in Figure 5c and Table S12 (Supporting Information). Despite the extended Th unit and the resulting enlarged E_g (Figure S17, Supporting Information), both BTP-FT and BTP-2FT exhibited reduced E_{loss} (0.523 and 0.564 eV, respectively) compared to BTP-4F (0.585 eV), contributing to a higher V_{oc} in the resulting devices. Notably, the lowest E_{loss} observed for BTP-FT arises from mitigations in both $\triangle E_2$ and $\triangle E_3$, facilitated by the appropriate incorporation of Th.

In the investigation utilizing EL spectroscopy and highly sensitive EQE (s-EQE), we observed a reduction in $\triangle E_2$ in the BTP-FT-based device, potentially associated with energy disorder. The latter is quantified by the Urbach energy parameter (E_u) following Urbach's rule, expressed as $\alpha(E) = \alpha_0 \times \exp((E-E_u)/E_0)$, where $\alpha(E)$ represents the absorption coefficient, α_0 and E_0 are constants, and E stands for photon energy. We determined the E_u values by fitting s-EQE curves[16] and found them as 23.17, 21.57, and 28.13 meV for PM6:BTP-4F, PM6:BTP-FT, and PM6:BTP-2FT, respectively (Figure 5d). A smaller E_u implies a lower energy disorder. The decrease in E_u validates the role of mitigating energy disorder in $\triangle E_2$ for the BTP-FT-based device. To elucidate the variations in $\triangle E_3$ among the three devices, direct measurements and comparison of their luminescence efficiency were conducted as depicted in Figure 5e. The resulting $\triangle E_3$ values were determined to be 0.254, 0.203, and 0.233 eV for BTP-4F, BTP-FT, and BTP-2FT, respectively. The variance in $q\triangle V_{oc}^{non\text{-}rad}$ contributes significantly to the differences in V_{oc} among the devices. Ultimately, due to the mitigations of both $\triangle E_2$ and $\triangle E_3$, the BTP-FT-based device exhibits a lower E_{loss}, consequently resulting in an increased voltage compared to the one based on the parental molecule. Thus, our strategy of incorporating a non-fused Th terminal effectively reduces E_{loss} by mitigating both radiative and non-radiative combination losses.

A higher V_{oc} in devices often indicates a lower driving force for charge separation and extraction, and a higher charge recombination probability, which significantly impacts J_{sc} and FF of PSCs. Therefore, we first explore the electronic properties at the

© 2025 The Author(s). Advanced Functional Materials published by Wiley-VCH GmbH

16163028, 2025, 24, Downloaded from https://advanced.onlinelibrary.wiley.com/doi/10.1002/adfm.202423137 by Statens Beredning, Wiley Online Library on [13/08/2025]. See the Terms and Conditions (https://onlinelibrary.wiley.com/terms-and-conditions) on Wiley Online Library for rules of use; OA articles are governed by the applicable Creative Commons License

acceptor–donor interfaces via DFT-based calculations across the three acceptor–donor configurations as presented in Figures 5g and S16 (Supporting Information). As the number of Th units increases, the energy gap between the local excited (LE) state and charge transfer (CT) state narrows (Table S13, Supporting Information), suggesting a reduced driving force for charge separation and extraction, and a higher likelihood of charge recombination. Consequently, this high V_{oc} achieved in the BTP-FT-based device without compromising J_{sc} and FF requires further study for a comprehensive understanding. To study the charge generation and exciton dissociation across the three PSCs, an investigation on the photocurrent density (J_{ph}) dependency on effective voltage (V_{eff}) was conducted. The probabilities of exciton dissociation and charge collection, denoted as P_d and P_c, were determined through J_{ph}/J_{sat} under short-circuit and maximal power output conditions, respectively.[17] As shown in Figure 5f, the calculated values ($P_{d/}P_c$) for devices based on BTP-4F, BTP-FT, and BTP-2FT were determined to be 95.56%/77.50%, 97.92%/86.59%, and 91.85%/74.03%, respectively. This highlights superior efficiency in exciton dissociation and charge collection in BTP-FT-based devices. which is consistent with the efficient photoluminescence quenching, as observed in the blend film (Figure S19, Supporting Information).

Next, the kinetics of charge recombination within the devices were investigated. As depicted in Figure 5i, we initiated measurements on the dependency of V_{oc} on light intensity (P_{light}). The slope of V_{oc} versus the natural logarithm of P_{light} is equal to kT/q, where k represents the Boltzmann constant, T is the temperature in Kelvin, and q is the elementary charge, bimolecular recombination predominates. If the slope > kT/q, the trap-assistant recombination is the dominant recombination mechanism.[18] The slopes obtained from PM6:BTP-4F, PM6:BTP-FT, and PM6:BTP-2FT devices were 1.10, 1.02, and 1.13, respectively, suggesting that trap-assisted recombination is effectively relieved in the device based on BTP-FT. Furthermore, we delved into the relationship between J_{sc} and P_{light}, which follows the equation $J_{sc} \propto {P_{light}}^{\alpha}$, where α is the exponential factor.[19] The α value for the BTP-FT-based device (0.98) exceeded those for the BTP-4F- (0.96) and BTP-2FT-(0.94) based ones (Figure 5h). An α value approaching 1 suggests a reduction in unfavorable bimolecular recombination. Hence, the BTP-FT-based device shows a lower level of bimolecular recombination, contributing to its highest J_{sc} and FF values generated. To further analyze the charge recombination characteristic, the transient photovoltage (TPV) was measured. As shown in Figure 5j, the carrier lifetime of BTP-FT-based PSC (2.19 µs) is much longer than those of PM6:BTP-4F (1.95 µs) and PM6:BTP-2FT (1.03 µs), confirming the effective suppression of charge recombination.[20] As shown in Figure 5k, the transient photocurrent (TPC) measurement was carried out to explore the charge extraction process in these devices. The shorter charge extraction time of 0.21 µs for PM6:BTP-FT (in comparison with 0.25 µs for BTP-4F and 0.51 µs for BTP-2FT) suggests that carrier extraction is faster in BTP-FT-based PSCs.[20]

The blend layers of BTP-FT demonstrated optimal phase separations conducive to efficient charge transport. Thus, we calculated their hole (μ_h) and electron (μ_e) mobilities,[21] as summarized in Table S14 (Supporting Information). For the PM6:BTP-4F, PM6:BTP-FT, and PM6:BTP-2FT-based blends, the μ_h/μ_e values were found to be $8.32 \times 10^{-4}/6.93 \times 10^{-4}$, $9.17 \times 10^{-4}/8.27 \times 10^{-4}$, and $3.01 \times 10^{-4}/1.64 \times 10^{-4}$ $cm^2 \cdot V^{-1} \cdot s^{-1}$, respectively. Both increased μ_h and μ_e values were observed for the blends from BTP-FT with the addition of the asymmetric Th substituent. Notably, BTP-FT-based devices achieved a more balanced μ_h/μ_e ratio of 1.11 compared to 0.69 for BTP-4F and 1.84 for BTP-2FT. These findings collectively suggest that the high and balanced charge carrier mobility can facilitate efficient charge transport, suppress charge recombination in the blend, and retain high FF and J_{sc} values in BTP-FT-based devices.

3. Conclusion

A mono- or di-thiophene unit is introduced to the terminals of the state-of-the-art SMA BTP-4F, yielding novel SMAs of asymmetric BTP-FT and symmetric BTP-2FT. A detailed study is performed to investigate the acceptor's molecular structures, configurations, intermolecular packings, solubilities, optical absorptions, surface energy, and calculated energy properties. When blended with the commonly used donor polymer PM6 for corresponding PSCs, a comprehensive set of characterization tools was used to investigate the thin film morphology, photovoltaic performance, charge carrier transports and recombination mechanisms, and electro- and photo-luminescent properties. Unexpectedly, it was proved that the noncovalent F···S interactions, rather than hydrogen bonding F···H, play a key role in determining molecular conformation as revealed by 2D NMR-NOESY measurements and delicate BAR-MD simulations. The strategic elevation of the LUMO energy level from −4.23 to −4.17 eV in asymmetric SMA BTP-FT, in combination with the reduced E_{loss}, leads to an enhanced V_{oc} of 0.900 V in PSCs. Devices based on BTP-FT exhibit reduced energetic disorder and improved luminescence efficiency in comparison with BTP-4F-based ones, demonstrating advantages in mitigating E_{loss} through both reduced radiative and non-radiative combination losses, thus contributing to an elevated device V_{oc}. In spite of a blueshifted light absorption compared to BTP-4F, BTP-FT did not compromise the J_{sc} of the device, resulting in a notable PCE of 17.56% in non-halogen-processed PM6:BTP-FT-based solar cells. Furthermore, the introduction of BTP-4F with a stronger near-infrared absorption as the third component further improved the PCE to 18.39% in the resulting ternary PSCs, one of the highest PCEs achieved from PSCs processed in non-halogenated solvents. Importantly, the asymmetric configuration created by introducing a Th moiety into electro-withdrawing EG groups effectively mitigates excessive aggregation and crystallinity, substantially enhancing solubility in toluene. This structural modification notably reduced the formation of large phase-separation domains within donor and acceptor blended films, thereby forming nanofibrillar morphology, promoting exciton dissociation, efficient charge transport, and suppressing charge recombination, ultimately augmenting the FF and J_{sc} in PSCs. Our results demonstrate that precise EG modification is an effective strategy to enhance the processability of resulting PSCs with such acceptors in non-halogen solvents, while also optimizing film morphology and improving photovoltaic device performance. This contribution diversifies efficient electron-withdrawing EGs and molecular design strategies in the field of organic electronics.

© 2025 The Author(s). Advanced Functional Materials published by Wiley-VCH GmbH

16163028, 2025, 24, Downloaded from https://advanced.onlinelibrary.wiley.com/doi/10.1002/adfm.202423137 by Statens Beredning, Wiley Online Library on [13/08/2025]. See the Terms and Conditions (https://onlinelibrary.wiley.com/terms-and-conditions) on Wiley Online Library for rules of use; OA articles are governed by the applicable Creative Commons License

Supporting Information

Supporting Information is available from the Wiley Online Library or from the author.

Acknowledgements

The authors thank the Swedish Research Council (2019-04683, 2020–05223), the Swedish Research Council Formas, The Knut and Alice Wallenberg Foundation (2022.0192, WISE), the Swedish Energy Agency (Grant number: P2021-90067, 45420–1) and STandUP for Energy collaboration. M.Z. and X.G. acknowledge financial support from Shandong Provincial Natural Science Foundation (ZR2022JQ09), Taishan Scholar Program at Shandong Province (tsqn202306061). The computations were enabled by resources provided by the National Academic Infrastructure for Supercomputing in Sweden (NAISS) and the Swedish National Infrastructure for Computing (SNIC) at Chalmers/C3SE and at the National Supercomputer Centre (NSC) at Linköping University, partially funded by the Swedish Research Council through grant agreements no. 2022–06725 and no. 2018–05973. J.W. further acknowledges the financial support from the Chinese Scholarship Council. Support from the Sino-Danish Center (SDC) for Education and Research is fully acknowledged.

Conflict of Interest

The authors declare no conflict of interest.

Data Availability Statement

The data that support the findings of this study are available from the corresponding author upon reasonable request.

Keywords

molecular conformation, non-fullerene acceptor, non-halogen solvent, polymer solar cell, power conversion efficiency

Received: November 26, 2024
Revised: December 26, 2024
Published online: January 19, 2025

[1] a) P. Cheng, G. Li, X. Zhan, Y. Yang, *Nat. Photonics* **2018**, *12*, 131; b) J. Hou, O. Inganas, R. H. Friend, F. Gao, *Nat. Mater.* **2018**, *17*, 119; c) G. Zhang, J. Zhao, P. C. Y. Chow, K. Jiang, J. Zhang, Z. Zhu, J. Zhang, F. Huang, H. Yan, *Chem. Rev.* **2018**, *118*, 3447; d) Z. Genene, W. Mammo, E. Wang, M. R. Andersson, *Adv. Mater.* **2019**, *31*, 1807275; e) J. Wang, P. Xue, Y. Jiang, Y. Huo, X. Zhan, *Nat. Rev. Chem.* **2022**, *6*, 614; f) K. Bini, D. Gedefaw, C. Pan, J. M. Bjuggren, A. Sharma, E. Wang, M. R. Andersson, *J. Appl. Poly. Sci.* **2019**, *136*, 47729.

[2] a) Y. Cui, Y. Xu, H. Yao, P. Bi, L. Hong, J. Zhang, Y. Zu, T. Zhang, J. Qin, J. Ren, Z. Chen, C. He, X. Hao, Z. Wei, J. Hou, *Adv. Mater.* **2021**, *33*, 2102420; b) J. Fu, P. W. K. Fong, H. Liu, C. S. Huang, X. Lu, S. Lu, M. Abdelsamie, T. Kodalle, C. M. Sutter-Fella, Y. Yang, G. Li, *Nat. Commun.* **2023**, *14*, 1760; c) Z. Gan, L. Wang, J. Cai, C. Guo, C. Chen, D. Li, Y. Fu, B. Zhou, Y. Sun, C. Liu, J. Zhou, D. Liu, W. Li, T. Wang, *Nat. Commun.* **2023**, *14*, 6297; d) W. Gao, F. Qi, Z. Peng, F. R. Lin, K. Jiang, C. Zhong, W. Kaminsky, Z. Guan, C. S. Lee, T. J. Marks, H. Ade, A. K. Jen, *Adv. Mater.* **2022**, *34*, 2202089; e) H. Liang, X. Bi, H. Chen, T. He, Y. Lin, Y. Zhang, K. Ma, W. Feng, Z. Ma, G. Long, C. Li, B. Kan, H. Zhang, O. A. Rakitin, X. Wan, Z. Yao, Y. Chen, *Nat. Commun.* **2023**, *14*, 4707; f) J. Wang, Y. Wang, P. Bi, Z. Chen, J. Qiao, J. Li, W. Wang, Z. Zheng, S. Zhang, X. Hao, J. Hou, *Adv. Mater.* **2023**, *35*, 2301583; g) J. Wang, M. Zhang, J. Lin, Z. Zheng, L. Zhu, P. Bi, H. Liang, X. Guo, J. Wu, Y. Wang, L. Yu, J. Li, J. Lv, X. Liu, F. Liu, J. Hou, Y. Li, *Energy Environ. Sci.* **2022**, *15*, 1585.

[3] S. Lee, D. Jeong, C. Kim, C. Lee, H. Kang, H. Y. Woo, B. J. Kim, *ACS Nano* **2020**, *14*, 14493.

[4] a) B. Walker, A. Tamayo, D. T. Duong, X. D. Dang, C. Kim, J. Granstrom, T. Q. Nguyen, *Adv. Energy Mater.* **2011**, *1*, 221; b) C. Liu, J. Liu, X. Duan, Y. Sun, *Adv. Sci. (Weinh)* **2023**, *10*, 2303842; c) R. Ma, X. Jiang, J. Fu, T. Zhu, C. Yan, K. Wu, P. Müller-Buschbaum, G. Li, *Energy Environ. Sci.* **2023**, *16*, 2316; d) M. Sun, K. N. Zhang, J. W. Qiao, L. H. Wang, M. Li, P. Lu, W. Qin, Z. Xiao, L. Zhang, X. T. Hao, L. Ding, X. Y. Du, *Adv. Energy Mater.* **2023**, *13*, 2203465; e) F. Sun, X. Zheng, T. Hu, J. Wu, M. Wan, Y. Xiao, T. Cong, Y. Li, B. Xiao, J. Shan, E. Wang, X. Wang, R. Yang, *Energy Environ. Sci.* **2024**, *17*, 1916.

[5] a) H. Lu, G. Ran, Y. Liu, Z. Pei, W. Liu, Y. Liu, Z. Tang, W. Zhang, Z. Bo, *Adv. Funct. Mater.* **2023**, *33*, 2301866; b) H. Bai, R. Ma, W. Su, T. A. D. Pena, T. Li, L. Tang, J. Yang, B. Hu, Y. Wang, Z. Bi, Y. Su, Q. Wei, Q. Wu, Y. Duan, Y. Li, J. Wu, Z. Ding, X. Liao, Y. Huang, C. Gao, G. Lu, M. Li, W. Zhu, G. Li, Q. Fan, W. Ma, *Nanomicro Lett* **2023**, *15*, 241; c) C. Yang, M. Jiang, S. Wang, B. Zhang, P. Mao, H. Y. Woo, F. Zhang, J. L. Wang, Q. An, *Adv. Mater.* **2024**, *36*, 2305356; d) M. Haris, Z. Ullah, S. Lee, D. H. Ryu, S. U. Ryu, B. J. Kang, N. J. Jeon, B. J. Kim, T. Park, W. S. Shin, C. E. Song, *Adv. Energy Mater.* **2024**, *14*, 2401597.

[6] a) Z. Abbas, S. U. Ryu, M. Haris, C. E. Song, H. K. Lee, S. K. Lee, W. S. Shin, T. Park, J.-C. Lee, *Nano Energy* **2022**, *101*, 107574; b) Z. Zhong, S. Chen, J. Zhao, J. Xie, K. Zhang, T. Jia, C. Zhu, J. Jing, Y. Liang, L. Hong, S. Zhu, D. Ma, F. Huang, *Adv. Energy Mater.* **2023**, *13*, 2302273.

[7] a) Z. Luo, H. Yan, C. Yang, *Acc. Mater. Res.* **2023**, *4*, 968; b) M. Yang, X. Tan, B. Yin, S. Kim, S. Pang, Z. Chen, X. Yang, C. Yang, Z. Liu, C. Duan, *ACS Energy Lett.* **2023**, *8*, 2641; c) H. Yao, J. Wang, Y. Xu, J. Hou, *Chem. Mater.* **2023**, *35*, 807; d) K. Yang, Q. Liao, C. W. Koh, J. Chen, M. Su, X. Zhou, Y. Tang, Y. Wang, Y. Zhang, H. Y. Woo, X. Guo, *J. Mater. Chem. A* **2019**, *7*, 9822; e) G. Li, X. Zhang, L. O. Jones, J. M. Alzola, S. Mukherjee, L. W. Feng, W. Zhu, C. L. Stern, W. Huang, J. Yu, V. K. Sangwan, D. M. DeLongchamp, K. L. Kohlstedt, M. R. Wasielewski, M. C. Hersam, G. C. Schatz, A. Facchetti, T. J. Marks, *J. Am. Chem. Soc.* **2021**, *143*, 6123; f) Y. Pan, X. Zheng, J. Guo, Z. Chen, S. Li, C. He, S. Ye, X. Xia, S. Wang, X. Lu, H. Zhu, J. Min, L. Zuo, M. Shi, H. Chen, *Adv. Funct. Mater.* **2021**, *32*, 2108614; g) X. Zhang, L. Qin, J. Yu, Y. Li, Y. Wei, X. Liu, X. Lu, F. Gao, H. Huang, *Angew. Chem. Int. Ed. Engl.* **2021**, *60*, 12475.

[8] a) G. Han, Y. Guo, L. Ning, Y. Yi, *Sol. RRL* **2018**, *3*, 1800251; b) Y. Shi, L. Zhu, Y. Yan, M. Xie, G. Liang, J. Qiao, J. Zhang, X. Hao, K. Lu, Z. Wei, *Adv. Energy Mater.* **2023**, *13*, 2300458.

[9] a) S. Refaely-Abramson, S. Sharifzadeh, M. Jain, R. Baer, J. B. Neaton, L. Kronik, *Phys. Rev. B* **2013**, *88*, 081204; b) L. R. Franco, C. Marchiori, C. M. Araujo, *J. Chem. Phys.* **2023**, *159*, 204110.

[10] a) J. Wu, Z. Ling, L. R. Franco, S. Y. Jeong, Z. Genene, J. Mena, S. Chen, C. Chen, C. M. Araujo, C. F. N. Marchiori, J. Kimpel, X. Chang, F. H. Isikgor, Q. Chen, H. Faber, Y. Han, F. Laquai, M. Zhang, H. Y. Woo, D. Yu, T. D. Anthopoulos, E. Wang, *Angew. Chem. Int. Ed. Engl.* **2023**, *62*, 202302888; b) J. Wu, F. Sun, X. Wang, Q. Chen, L. R. Franco, X. Zheng, C. M. Araujo, R. Yang, D. Yu, E. Wang, *Adv. Sci.* **2024**, *11*, 2406772.

[11] M. Chatzopoulou, R. F. Martínez, N. J. Willis, T. D. W. Claridge, F. X. Wilson, G. M. Wynne, S. G. Davies, A. J. Russell, *Tetrahedron* **2018**, *74*, 5280.

[12] X. Xia, L. Mei, C. He, Z. Chen, N. Yao, M. Qin, R. Sun, Z. Zhang, Y. Pan, Y. Xiao, Y. Lin, J. Min, F. Zhang, H. Zhu, J.-L. Bredas, H. Chen, X.-K. Chen, X. Lu, *J. Mater. Chem. A* **2023**, *11*, 21895.

© 2025 The Author(s). Advanced Functional Materials published by Wiley-VCH GmbH

16163028, 2025, 24, Downloaded from https://advanced.onlinelibrary.wiley.com/doi/10.1002/adfm.202423137 by Statens Beredning, Wiley Online Library on [13/08/2025]. See the Terms and Conditions (https://onlinelibrary.wiley.com/terms-and-conditions) on Wiley Online Library for rules of use; OA articles are governed by the applicable Creative Commons License

[13] a) N. Yao, Q. Fan, Z. Genene, H. Liu, Y. Xia, G. Wen, Y. Yuan, E. Moons, J. van Stam, W. Zhang, X. Lu, E. Wang, F. Zhang, *Sol. RRL* **2023**, *7*, 2201134; b) J. Wang, Y. Wang, P. Bi, Z. Chen, J. Qiao, J. Li, W. Wang, Z. Zheng, S. Zhang, X. Hao, J. Hou, *Adv. Mater.* **2023**, *35*, 2301583.
[14] D. K. Owens, R. C. Wendt, *J. Appl. Poly. Sci.* **2003**, *13*, 1741.
[15] L. Zhan, S. Li, Y. Li, R. Sun, J. Min, Z. Bi, W. Ma, Z. Chen, G. Zhou, H. Zhu, M. Shi, L. Zuo, H. Chen, *Joule* **2022**, *6*, 662.
[16] F. Sun, X. Wang, M. Wan, Z. Liu, Y. Luo, J. Ren, X. Zheng, T. Rath, C. Xiao, T. Hu, G. Trimmel, R. Yang, *Adv. Funct. Mater.* **2023**, *33*, 2306791.
[17] J. L. Wu, F. C. Chen, Y. S. Hsiao, F. C. Chien, P. Chen, C. H. Kuo, M. H. Huang, C. S. Hsu, *ACS Nano* **2011**, *5*, 959.
[18] L. J. A. Koster, V. D. Mihailetchi, R. Ramaker, P. W. M. Blom, *Appl. Phys. Lett.* **2005**, *86*, 123509.
[19] M. Lenes, M. Morana, C. J. Brabec, P. W. M. Blom, *Adv. Funct. Mater.* **2009**, *19*, 1106.
[20] X. Song, K. Zhang, R. Guo, K. Sun, Z. Zhou, S. Huang, L. Huber, M. Reus, J. Zhou, M. Schwartzkopf, S. V. Roth, W. Liu, Y. Liu, W. Zhu, P. Muller-Buschbaum, *Adv. Mater.* **2022**, *34*, 2200907.
[21] C. M. Proctor, C. Kim, D. Neher, T. Q. Nguyen, *Adv. Funct. Mater.* **2013**, *23*, 3584.

© 2025 The Author(s). Advanced Functional Materials published by Wiley-VCH GmbH

16163028, 2025, 24, Downloaded from https://advanced.onlinelibrary.wiley.com/doi/10.1002/adfm.202423137 by Statens Beredning, Wiley Online Library on [13/08/2025]. See the Terms and Conditions (https://onlinelibrary.wiley.com/terms-and-conditions) on Wiley Online Library for rules of use; OA articles are governed by the applicable Creative Commons License